Mesospheric gravity wave activity estimated via airglow imagery, multistatic meteor radar, and SABER data taken during the SIMONe–2018 campaign

Fabio Vargas[1], Jorge L. Chau[2], Harikrishnan Charuvil Asokan[2,3], and Michael Gerding[2]

[1]Department of Electrical and Computer Engineering, University of Illinois at Urbana-Champaign, Urbana, IL, USA, 61801
[2]Leibniz Institute of Atmospheric Physics and the University of Rostock, Kühlungsborn, Germany, 18225
[3]Laboratoire de Mécanique des Fluides et d'Acoustique, CNRS, École Centrale de Lyon, Université Claude Bernard Lyon 1, INSA de Lyon, Écully, France

Correspondence: Fabio Vargas (fvargas@illinois.edu)

Abstract. We describe in this study the analysis of small and large horizontal scale gravity waves from datasets composed of images from multiple mesospheric nightglow emissions as well as multistatic specular meteor radar (MSMR) winds collected in early November 2018, during the SIMONe–2018 campaign. These ground-based measurements are supported by temperature and neutral density profiles from TIMED/SABER satellite in orbits near Kühlungsborn, northern Germany (54.1°N, 11.8°E). The scientific goals here include the characterization of gravity waves and their interaction with the mean flow in the mesosphere and lower thermosphere and their relationship to dynamical conditions in the lower and upper atmosphere. We obtain intrinsic parameters of small and large horizontal scale gravity waves and characterize their impact in the mesosphere region via momentum flux and flux divergence estimations. We have verified that a small percent of the detected wave events are responsible for most of the momentum flux measured during the campaign from oscillations seen in the airglow brightness and MSMR winds. From the analysis of small-scale gravity waves in airglow images, we have found wave momentum fluxes ranging from 0.38 to 24.74 m^2/s^2 (0.88±0.73 m^2/s^2 on average), with a total of 586.96 m^2/s^2 (sum over all 362 detected waves). However, small horizontal scale waves with flux >3 m^2/s^2 (11% of the events) transport 50% of the total measured flux. Likewise, wave events having flux >10 m^2/s^2 (2% of the events) transport 20% of the total flux. The examination of two large-scale waves seen simultaneously in airglow keograms and MSMR winds revealed relative amplitudes >35%, which translates into momentum fluxes of 21.2–29.6 m^2/s^2. In terms of gravity wave–mean flow interactions, these high momentum flux waves could cause decelerations of 22–41 m/s/day (small-scale waves) and 38–43 m/s/day (large-scale waves) if breaking or dissipating within short distances in the mesosphere and lower thermosphere region. The dominant large-scale waves might be the result of secondary gravity excited from imbalanced flow in the stratosphere caused by primary wave breaking.

Copyright statement. TEXT

1 Introduction

20

Atmospheric gravity waves represent a class of atmosphere oscillations where buoyancy is the restoring force. This class of waves transport momentum and energy over large distances within the atmosphere and have as primary sources troposphere disturbances like flow over topography, convective systems, or jets (e.g., Vincent and Alexander, 2020). To preserve kinetic energy, the amplitudes of the gravity waves grow nearly exponentially as they propagate upward into less dense air at higher

25 altitudes. Because these waves break and dissipate, they deposit their momentum and energy into the background atmosphere. This successively affects the atmosphere over a broad range of scales, from local generation of turbulence to forcing of large-scale circulation (Fritts and Alexander, 2003; Vincent and Alexander, 2020).

This dynamical forcing is most prominent within the mesosphere and lower thermosphere (MLT) at altitudes of typically 50–130 km. Within this range, a large fraction of upward-propagating gravity waves reach their maximum amplitudes and

30 break. The resulting dynamical forcing causes a global-scale circulation within the mesosphere with strong upwelling within the summer polar region and downwelling within the winter polar region (Houghton, 1978; Holton, 1984). Adiabatic cooling and heating connected to this circulation cause thermal conditions within the mesosphere to deviate far away from radiative equilibrium (Solomon et al., 1987; Vargas et al., 2015).

The role of gravity waves is further complicated as they interact with the background flow as they propagate through the

35 atmosphere. This results in an altitude-dependent filtering of the gravity wave spectrum by the background wind, planetary and tidal waves. The gravity wave spectrum reaching higher altitudes thus carries an imprint of the dynamics at lower altitudes. Interactions between gravity waves and the mean flow and subsequent wave breaking then generate secondary waves within the mesosphere that propagate both upward and downward. This happens through the creation of temporally and spatially localized momentum and energy fluxes, which successively create strong local body forces and flow imbalances which then

40 excite the secondary waves (Fritts et al., 2006; Vargas et al., 2016; Vadas et al., 2018; Vadas and Becker, 2018; Becker and Vadas, 2018).

While today the essential nature of the wave-driven circulation of the middle atmosphere is known, important mechanisms and interactions remain to be quantified. Most notably, this concerns wave sources, wave dissipation, and therefore the resulting forcing of the mean flow. A decisive quantity to be specified is the directional momentum flux, including its altitude dependence

45 and its spectral distribution with reference to horizontal and vertical wavelengths.

With the objective of bridging these gaps in gravity wave dynamics while estimating their momentum flux, an observation campaign named SIMONe–2018 (Spread-spectrum Interferometric Multi-static meteor radar Observing Network) was carried out in early Nov. 2018, to collect a large number of specular meteor echoes from several locations (e.g., Vierinen et al., 2019; Asokan et al., 2020). Also, an all-sky airglow imager system running out of the Leibniz Institute of Atmospheric Physics,

50 Kühlungsborn, Germany, was observing the region in parallel to provide image data of the mesosphere and the horizontal structure of atmospheric oscillations during the campaign.

SIMONe–2018 campaign measurements permit the study of the spatial and temporal modes of gravity waves perturbing the background wind and the airglow simultaneously. In this paper, we have analyzed all-sky imager (ASI) airglow images

and multistatic specular meteor radar (MSMR) wind data to access short and large-scale gravity wave dynamics using distinct

55   methods for different wave categories. Airglow images are processed directly using an auto-detection method for small-scale, short-period (<1 hour) gravity waves aided by MSMR background wind measurements for Doppler correction of the wave periods. For nights presenting obvious large-scale, long-period (>1 hour) oscillations, wave features are studied via direct examination of large amplitude filtered wind fluctuations and airglow keogram spectral analysis. We have also obtained measurements of the neutral density, temperature, and OH emission volume emission rates from SABER aboard the NASA TIMED

60   (Thermosphere, Ionosphere, Mesosphere Energetics and Dynamics) satellite (http://saber.gats-inc.com) to determine the state of the mesosphere region near the observatory during the campaign. This study shows remarkable instances of waves perturbing the airglow and the wind, providing a singular opportunity to examine the linear gravity wave theory's predictions and the occurrence of gravity waves perturbing multiple mesospheric quantities simultaneously.

2   Instrumentation and Data

65   ### 2.1   All-sky airglow imager (ASI)

The Boston University all-sky imager was deployed in late 2016 at the Leibniz Institute of Atmospheric Physics (IAP) in Kühlungsborn, Germany. The data collected is available for visualization at http://sirius.bu.edu/data/, and raw images are available by direct request to the authors. The IAP all-sky imager system is equipped with six interference filters enabling the observation of four mesosphere nightglow emissions with a background filter for the hydroxyl emission. A filter for the

70   thermospheric redline (at 630.0 nm) is also available, but images of this emission were not taken during SIMONe–2018 due to filter technical issues. The specifications of filter wavelengths and integration times are in Table 1. Emission altitudes are discussed in Section 2.3.

     The SIMONe–2018 campaign was carried out for more than a week, but clear skies were seen only during four nights, which limited the optical observations with the all-sky imager. The sky conditions for the four clear nights are summarized in Fig. 1

75   by zonal and meridional keograms of the $O(^1S)$ emission. Although only keograms of the $O(^1S)$ emission are shown here, we have also built keograms for the other three mesospheric emissions, which are available as accompanying files of this paper. Keograms are built from raw or preprocessed airglow images depending on what wave information we want to retrieve. For the zonal keogram, the vertical scale indicates west (negative) and east (positive), while the vertical scale in meridional keograms indicates south (negative) and north (positive). The horizontal scale in both zonal and meridional keograms refers to universal

80   time. Notice the center of vertical axis of the keograms corresponds to the brightness registered by the zenith pixel localized at the center of the images. For a detailed explanation of keograms from airglow images, the reader is referred to Vargas et al. (2020).

     The left side panels of Fig. 1 show keograms built directly from $O(^1S)$ raw, dewarped images. The keograms' contrast was optimized to show brightness variation features present throughout the night. Evident long period oscillations seen in

85   the airglow brightness on Nov. 3–4 and Nov. 6–7 are associated with large-scale, long horizontal wavelength gravity waves perturbing the greenline layer. For instance, notice in the meridional keogram of Nov. 3–4 the orientation of the brightness

variation associated with a large-scale wave in a region tilted from top to bottom during 1930 UTC to 2230 UTC, indicating a coherent oscillation traveling from north to south. The tilt in the brightness region is not pronounced in the zonal keogram in the same time span and indicates the wave horizontal vector has a small, negligible component in the west-east direction.

90 Perturbations of the same nature are also seen in the O_2 and OH emissions for the same nights.

The right side panels of Fig. 1 show zonal and meridional keograms of the same clear nights built using time-difference airglow images. Time-difference operation involves subtracting an image from the previous one (same emission) with the goal of filtering out long-term variations in the airglow brightness (e.g., Swenson and Espy, 1995; Tang et al., 2005; Vargas et al., 2016). The result is an image where the contrast of short-period, small-scale oscillations is enhanced. These small-scale waves

95 show up in the keograms as tilted bright/dark bands. Because long periods are eliminated, time-difference keograms permit rapid access to the activity of short period waves each night.

2.2 Multistatic specular meteor radar

During the SIMONe–2018 campaign, MSMR measurements were obtained during seven days continuously. Briefly, the campaign consisted of 14 multistatic links that were obtained by using two pulse transmitters located in Juliusruh (54.63°N,

100 13.37°E) and Collm (51.31°N, 13.00°E), respectively, and one coded-continuous wave transmitter located in Kühlungsborn. Eight receiving sites, receiving the scattered signal of at least one transmitter, were used. This campaign combines the multistatic approach called MMARIA (Multistatic Multifrequency Agile Radar Investigations of the Atmosphere) (Stober and Chau, 2015) with the SIMONe (Spread Spectrum Interferometric Multistatic meteor radar Observing Network) concept (Chau et al., 2019). In the latter case a combination of spread-spectrum, multiple-input multiple-output, and compressing sensing radar

105 techniques is implemented (Vierinen et al., 2016; Urco et al., 2018, 2019). The winds used in this work have been obtained with a gradient method, i.e., besides the mean horizontal and vertical winds, the gradients of the horizontal components have also been obtained (Chau et al., 2017). Data from one day of this campaign has been used to test a second-order statistics approach by Vierinen et al. (2019). More details of the SIMONe–2018 campaign as well as results of second-order statistics are given in the accompanying paper of this publication (see Asokan et al., 2020).

110 Here, we have used the MSMR winds in combination with the airglow data to give a full characterization of the gravity wave dynamics observed during the campaign. Fig. 2 shows the (a) zonal and (b) meridional winds in the range of 75 to 105 km measured during SIMONe–2018. The dashed boxes indicate the hours of combined airglow observations in the night time. The background wind is dominated by 12 hours of tidal oscillations presenting maximum amplitudes larger than 50 m/s, but spectral analysis reveals the presence of higher tidal harmonics of 8 and 6 hours (see Fig. 6 and Fig. 7).

115 Fig. 2 also presents filtered (c) zonal and (d) meridional winds calculated using a five-hour high-pass filter. The filtered winds indicate the presence of smaller period gravity waves perturbing simultaneously the background wind and the airglow. For instance, see the filtered meridional wind (Fig. 2d) on Nov. 3–4 that shows a coherent oscillation (red ellipse) throughout the night. This oscillation is also evident in the airglow brightness variation (meridional keogram in Fig. 1c) during the same night.

2.3 Satellite data (TIMED-SABER)

We have also collected observations of the SABER instrument on board the TIMED satellite within four degrees from the observation site (Fig. 3). SABER profiles used here are presented in Fig. 4a–c, while Fig. 4d shows the calculated volume emission rate of the mesosphere airglow emissions as explained below. The thick lines in Fig. 4 indicate the mean of corresponding individual profiles (dotted lines) for the various orbits of the satellite during the campaign. The corresponding orbits are specified in the legend of each chart.

From Fig. 4a, we can verify that the atmosphere is stable once the atmosphere lapse rate is larger than the adiabatic lapse rate in the altitude range of 88-99 km. The lapse rate is even positive below and above that range. Even though the satellite orbits registered during SIMONe–2018 were not exactly over the observatory, they are within the field of view of the imager (Fig. 3). Thus, there is a good chance the background atmosphere above the observation site is similar to that indicated by SABER (Fig. 4), although the temperature might still be influenced by gravity waves once we have averaged only a few profiles. Because of that, we are confident using SABER background profiles to make inferences about the propagation conditions for the waves seen over the observatory.

Fig. 4d corresponds to our estimation of volume emission rate (VER) profiles for the OH, O_2, and $O(^1S)$ airglow emissions. These VER profiles were calculated using the mean temperature, atomic oxygen, molecular oxygen, and molecular nitrogen profiles in Fig. 4a–b along with the reaction rates of each emission from Vargas et al. (2007). The characteristics of each layer (measured and calculated VERs) are obtained from a Gaussian model (thin lines in Fig. 4d) to fit each profile from which we obtain the layer peak, width, and FWMH. The mean characteristics of the airglow layers are presented in Table 2. The goodness of fitting scores $R^2 > 0.95$ for all five VER curves. The layer centroids, obtained by estimating $\frac{\int z \, \mathrm{VER} dz}{\int \mathrm{VER} dz}$, are in general a few kilometers above the estimated layer peaks because of departures of the actual VER vertical structure from the Gaussian fitting model.

3 Data Analysis and Results

A full characterization of the gravity wave field requires knowledge of the background wind over the observation site. The significant background wind acting in the vicinity of an airglow layer is a function of the vertical structure of the emission (the volume emission rate) that has finite thickness (see Fig. 4d). We take that into account in this study by calculating the weighted background wind (Fig. 6a–c) by using the individual volume emission rate of each layer as weighting functions. The weighted wind expression for a given VER is $(u_w, v_w) = \frac{\int (u,v) \, \mathrm{VER} dz}{\int \mathrm{VER} dz}$, where u_w and v_w are the weighted zonal and meridional winds (Fig. 6), respectively. Notice that the weighted winds are still a function of time.

3.1 Short-scale gravity wave analysis

The majority of waves observed during SIMONe–2018 are of short-scale, fast oscillations presenting periods of less than one hour. The keograms of Fig. 1 (right panels) show the most prominent waves of this category registered during the clear nights

of the campaign. These short-scale gravity waves are analysed here using the auto-detection method (Tang et al., 2005; Vargas et al., 2009; Vargas, 2019).

The auto-detection method uses a set of three sequential frames of an emission to detect the gravity wave content around the acquisition time of the central frame. We repeat this procedure for all the images taken throughout the night grouped into several sets of three sequential frames. From each set, two time-difference (TD) images are obtained and the cross-spectra of the set are calculated from these two TD images (see Fig. 1 in Vargas et al., 2009). We then obtain the wavenumber coordinates (k_x, k_y) of dominant peaks in the cross-spectra periodogram as well as the phase $\delta\phi$ of these peaks from the phase periodogram at the same peak coordinates. The horizontal wavelength λ_h and the wave orientation θ are calculated using the spectral position (k_x, k_y). The phase velocity and period are retrieved using $\delta\phi$ and λ_h of each peak along with $\delta t = 10$ minutes, the filter wheel cycle period (see Fig. 2 in Vargas, 2019). We then obtain the vertical wavelength from the gravity wave dispersion relation for high frequency waves.

Fig. 5 shows the results from the auto-detection method for all the emissions recorded during SIMONe–2018. Unfiltered, weighted background winds of Fig. 6a–c were used to carry out the Doppler shift correction on observed wave periods. Thus, the parameters shown correspond to intrinsic properties of the waves. The top-center box in Fig. 5 contains a summary of statistics of the wave parameters measured. Fig. 5e shows vertical wavelengths ranging from 10 to 30 km, while horizontal wavelengths in Fig. 5m cluster around 75–125 km. Waves transporting large momentum flux are mainly oriented towards Northwest and Southwest (Fig. 5a), but the polar histogram in Fig. 5f shows a large number of waves traveling southeastward into the dominant wind orientation (Fig. 5k). The estimated intrinsic periods shown in Fig. 5e range within 20–40 min, with intrinsic phase speeds in the interval of 30-80 m/s in the campaign (Fig. 5b). The largest wave relative amplitude estimated from the images is 7% in Fig. 5d, but this does not necessarily translate into large momentum flux waves, which depends on other wave parameters.

Because of the ASI long integration times (two minutes/image) and filter wheel cycle (10 minutes), we have detected only waves of periods longer than 20 minutes. However, as we fully characterize the intrinsic parameters of every wave captured by the auto-detection method, we were able to estimate the momentum flux of the observed events (e.g., Vargas et al., 2007). Fig. 5l shows the daily momentum flux detections over the length of the campaign, with larger momentum flux waves appearing on Nov. 2–3 and Nov. 3–4. The momentum flux vs. intrinsic wave period chart (Fig. 5g) reveals a tendency of larger period waves carrying larger momentum fluxes. Conversely, Fig. 5h (Fig. 5i) reveals that large horizontal (vertical) wavelength waves transport less momentum flux.

3.2 Large-scale gravity wave analysis

During SIMONe–2018, we have also observed the presence of large-scale gravity waves modulating simultaneously the airglow brightness keograms (Fig. 1c and 1e) and the horizontal wind (Fig. 2c and 2d). To study these large-scale oscillations in the wind at the altitude of the airglow, we have calculated the wind fluctuations weighted by the volume emission rate of each layer (Fig. 6d–f). The dashed boxes represent the periods of simultaneous operation of the MSMR and ASI systems.

The weighted wind fluctuations are similar in each layer once the layers peak within ± 2 km from each other (see Table 2)

185 and are thicker than expected with mean FWHM of 15 km (e.g., Greer et al., 1986; Gobbi et al., 1992; Melo et al., 1996). Thus, the overlap of the VER profiles is non-negligible and the rms values of the filtered winds are expected to have similar magnitude. The calculated rms magnitudes are 6.9 ± 1.0 m/s and 5.9 ± 0.9 m/s in the zonal direction and meridional directions, respectively.

The spectral content of the weighted wind fluctuations is shown in Fig. 7. Several tidal harmonics are still present in the

190 spectra due to energy leakage (vertical dotted red lines in Fig. 7) even after wind filtering carried out to remove periods larger than 5 hours. However, there are a few persisting peaks that we attribute to gravity waves. For instance, the peaks in the vicinity of 0.21 cycles/hour (zonal direction) and 0.24 cycles/hour (meridional direction) are seen clearly in the wind fluctuation of Nov. 3–4. The spectra of the fluctuations show a salient peak near 0.11 cycles/hour (zonal and meridional directions), corresponding to a wave of 8.9 ± 1.0 hours that can be seen in the keograms of Nov. 6–7, 2018, close to the peak of the 12 hour period

195 associated with the semidiurnal atmospheric tide. A hodograph analysis of the filtered winds must be carried out in a separate work to clarify the nature of the dominant peaks shown in Fig. 7.

We have analysed the wind fluctuations against obvious wave features present in the keograms of Nov. 3–4 and Nov. 6–7. We carry out this analysis by overlapping the $O(^1S)$ weighted wind fluctuations on top of the corresponding keograms for these two observation nights (Fig. 8).

200 On Nov. 3–4, a strong, coherent feature presenting period of 4 ± 1 hours is observed in the meridional wind indicated by the dashed black lines. As the meridional wind peaks, the meridional keogram brightness dims (Fig. 8a); as the meridional wind decreases and reverses direction, the airglow brightens. Both zonal and meridional keograms present an enhanced brightness at 2100 UTC, but a second brightness peak in the airglow is only seen near the edges of the meridional keogram later on at 0100 UTC (Fig. 8a bottom). The meridional keogram shows a tilt in the brightness structure between 1900 and 2100 UTC

205 that indicates a wave is traveling southwards. In the same time span, the zonal keogram has no obvious tilt in the enhanced brightness, suggesting no wave propagation in the east-west direction. The filtered zonal wind confirms this as it shows a quite distinct and incoherent wind variation compared to that in the meridional direction. We have also verified, by visual inspection of the images, that this wave horizontal structure does not fit within the airglow image field of view (512×512 km^2) and is only noticeable via keogram analysis.

210 Similarly, we have also observed enhancements in the airglow brightness on Nov. 6–7 (dashed black lines) associated with a large-scale wave with period longer than $\sim8\pm1$ hour. The wave activity, evident in the weighted wind fluctuations (Fig. 8b), coincides well with the $O(^1S)$ airglow enhanced brightness in the zonal keogram of Nov. 6–7 around 0000 UTC. This brightness enhancement shows a slight tilt that indicates a wave propagating from west to east. The negligible tilt of the airglow brightness in the meridional keogram implies the wave has no evident north-south component.

215 A spectral analysis of the keograms of Nov. 3–4 and Nov. 6–7 in Fig. 9 enables finding the zonal (k_x) and meridional (k_y) wavenumber, which are components of the horizontal wavenumber as $k_h = \sqrt{k_x^2 + k_y^2}$, while the wave observed frequency is $\omega_o = \frac{2\pi}{\tau_o}$. We show the zonal and meridional keogram spectra for Nov. 3–4 in Fig. 9a and c, and for Nov. 6–7 in Fig. 9b and d.

For Nov. 3-4, the zonal keogram spectrum indicates a peak at $k_x = 0.0 \times 10^{-3}$ cycles/km and $\omega_o = -0.17$ cycles/hours (observed period τ_o =5.7±1.0 hour), where the negative sign is associated with a forward evolving time. The meridional keogram spectrum indicates a dominant peak at $\omega_o = -0.21$ cycles/hour (τ_o =4.6±1.0 hour) and meridional wavenumber $k_y \sim -0.7 \times 10^{-3}$ cycles/km ($\lambda_y \sim$1365 km), where the negative sign indicates a southward-propagating wave. The horizontal scale of the wave in the meridional direction is twice as large as the mapped image FOV (512x512 km^2), thus the horizontal wave structure is hardly fully seen in single airglow image. The large-scale wave occurring on Nov 6–7 is represented in the zonal spectrum by the peak near $\omega_o \sim -0.11$ cycles/hour (τ_o =9.1±1.0 hour) and $k_x \sim 0.2 \times 10^{-3}$ cycles/km ($\lambda_x \sim$4100 km). The positive sign in (k_x) indicates an eastward-propagating wave. The meridional keogram spectrum indicates a peak at the same frequency, but with $k_y \sim 0$ cycles/km, indicating no propagation of the wave in the meridional direction.

We show in Fig. 10 the time-altitude cross section of the weighted zonal and meridional wind fluctuations for the nights of Nov. 3–4 and Nov. 6–7, respectively. The downward phase progression of the large-scale waves observed in the time-altitude cross section for these two nights can be verified straightforwardly, which enables deriving the vertical wavelength and the period of these wave events, and also verifying that these waves are propagating upwards. We have drawn continuous (dotted) white lines on top of the crests (troughs) of the salient wave structures to help guide the eye while estimating the vertical wavelength and period of the structures. The lines were drawn only on top of the meridional wind (Nov. 3–4) and zonal wind (Nov. 6–7) cross sections where the wave structures are well defined. We estimate from these lines a vertical wavelength of λ_z =25.6±1.0 km and a period of τ_o =4.3±1.0 hours for the wave seen on Nov. 3–4, while for the wave seen on Nov. 6–7, we estimate a period of τ_o =8.0±1.0 hours and a vertical wavelength of λ_z =21.3±1.0 km. The periods derived here from the descending phase analysis are consistent with those derived from the keogram spectral analysis above.

4 Discussion

The propagation conditions for gravity waves during SIMONe–2018 are depicted in Fig. 4 showing the temperature and constituent densities over the observatory. While the vertical structures of the atomic oxygen density appear normal, the mean temperature indicates convectively favorable conditions for gravity waves vertical propagation, as the ambient lapse rate is positive below $\sim$87 km and above $\sim$99 km. Within 86–98 km range, the ambient lapse rate is negative but still sub-adiabatic, and convective instabilities are unlikely to form under these conditions. Thus, gravity wave dissipation due to convective instabilities would not affect the vertical evolution of the gravity wave field during the campaign. Conversely, because the horizontal winds occasionally have relatively large amplitudes of >50 m/s (Fig. 2a and Fig. 2b), the wind field could cause critical levels where waves are absorbed or reflected. Waves having specific sets of intrinsic parameters would hardly propagate beyond these critical level altitudes.

We can verify the effect of background wind on the propagation direction of the waves by examining Fig. 5. The momentum flux vs. propagation direction chart (Fig. 5a) shows a number of waves with large momentum flux oriented towards northwest and southwest, while Fig. 5k shows a dominant southeastward wind during SIMONe–2018 observations. Thus, it is likely that the background wind is controlling the propagation of southeastward waves via dynamic filtering. However, the wave

propagation direction histogram (Fig. 5f) indicates that a significant number of waves still propagate into the wind. These waves must then have horizontal phase speed larger than the background wind speed. In fact, we have estimated an average phase speed of 56.6±13.6 m/s for waves traveling in southeast quadrant, while wind has magnitude of 39.3±18.9 m/s in the same direction. This suggests these fast waves were able to overcome critical levels as propagating vertically.

255   Horizontal wavelengths, intrinsic periods, phase speeds, and vertical wavelengths of waves detected during SIMONe–2018 are directly comparable with the results of Li et al. (2011), which used a similar auto-detection method to analyze short-period, fast gravity waves in the airglow. Our statistics show an average vertical wavelength of 18.5±4.6 km, which is compatible with the results of Li et al. (2011) showing vertical wavelengths clustering from 20 to 30 km. They have shown horizontal wavelengths clustering around 15–30 km, while our results peak around 75–100 km. Fast waves reported here present remarkably

260   larger horizontal scales than those of Li et al. (2011), which could be associated with the location and type of terrain (Maui–sea vs. IAP–land) and gravity wave sources acting near the observatories. Yet, our sample is representative of the winter solstice conditions observed for a week, while that from Maui is representative of the season conditions observed over five years.

There are obvious discrepancies in intrinsic periods estimated in this study against those of Li et al. (2011). Observe that here the bulk of periods range from 20 to 30 min, while Li et al. (2011) report 77% of waves having periods of <10 min. We

265   attribute this discrepancy to the different integration time and the filter wheel cycle of the observing airglow camera systems; during SIMONe–2018, we have observed several emissions with a filter wheel cycle of 10 min, which allows us to detect wave periods longer than 20 min only. Li et al. (2011) used a filter wheel cycle of two min while observing a single emission, which allows the detection of waves of time scales as short as ∼5–6 min, the Brunt-Vaisala period near the mesopause. The filter wheel cycle time seems to affect other parameters as well. For instance, while Li et al. (2011) report a majority of wave

270   intrinsic phase speeds in the range of 50–100 m/s, we estimated slower intrinsic phase speeds of 31.2±17.3 m/s.

In another study, Li (2011) used one year of OH airglow observations over the Andes Lidar Observatory (ALO) in South America to characterize small-scale, fast gravity waves. He found that the peak of distribution of horizontal wavelength falls in the range 20–30 km, intrinsic phase speed ranges mainly 40–100 m/s (peak at 70 m/s), intrinsic periods of 80% the population fall in the range 5–20 min, and vertical wavelengths distribution peaks around 15 km. These results resemble those of Maui,

275   and the same discrepancies from the results in SIMONe–2018 are applicable. However, the sources of waves over the South American observatory are much clearer and related with convection in central Argentina to the east of ALO. These sources generate fast, short period, small horizontal scale waves that can be captured over the ALO imager. The farther away the source, the fewer short periods seen, which explains a secondary peak in the horizontal wavelength distribution of Li (2011) occurring around 80–110 km. This range is comparable to the distribution of horizontal wavelengths from the SIMONe–2018

280   campaign showing that a peak around 75–100 km would be related with tropospheric convective sources active far from the IAP observatory.

The momentum flux of these high-frequency waves detected during SIMONe–2018, which are seen in Fig. 5, is calculated using the methodology described in Vargas et al. (2007). The momentum flux shows a larger component towards the west of -0.36±1.51 m²/s² on average, while the northward meridional component is one sixth that magnitude. Ignoring for a moment

285   the wave propagation direction, the mean momentum flux is 0.88±0.73 m²/s². For all the 362 waves detected during SIMONe–

Atmospheric
Chemistry
and Physics
Discussions

2018, the total momentum is 586.96 m^2/s^2, where 50% of this total is due to waves carrying flux > 3 m^2/s^2 (40 events). Thus, 11% of the waves are responsible for carrying 50% of the momentum flux estimated from our auto-detection method during the campaign.

In spite of the small mean value, momentum flux bursts between 10 and 30 m^2/s^2 were mainly seen in the O$_2$ emission during the campaign. These highly energetic waves were traveling northwestward, presenting intrinsic periods of 30–40 min, horizontal wavelength of ~90 km, and vertical wavelength of 12–15 km (see charts of each emission in the supporting files accompanying this publication). The sum of momentum flux of these waves (8 events) accounts for 20% of the total momentum flux measured during the campaign for small-scale waves. It is not clear why the enhanced waves are seen most in the O$_2$ emission once the layer's peaks nearly overlap.

We see that even in smaller numbers, the more energetic, larger momentum flux waves could have greater impact in the atmosphere. For instance, noticing Fig. 9e of Vargas et al. (2007), one can verify that waves carrying momentum flux larger than 3 m^2/s^2 would potentially cause a drag larger than 22–41 m/s/day, considering the wave breaking continues for 24 hours, which would lead to considerable mean flow deceleration and body forces capable of exciting secondary waves as point-like sources (Vadas and Becker, 2018). For example, by considering the primary wave source and wave breaking mechanism in a given altitude acting for four hours (about half of a typical nighttime observation period), we estimate a potential deceleration in the mean flow of 3.7–6.8 m/s in the same time span (four hours) caused by the breaking of the primary wave.

We have estimated the observed horizontal wavelength and frequency parameters of the large-scale waves shown in the airglow (Fig. 8) using the spectrum of the zonal and meridional keograms in Fig. 9. We can combine the observed frequency with the observed unfiltered background wind to derive the intrinsic period of the waves using $\omega = \omega_o - \mathbf{k_h} \cdot \mathbf{v}$ (Doppler correction), where ω_o is the frequency measured by an observer on the ground, $\mathbf{k_h} = (k_x, k_y)$ and $\mathbf{v} = (u, v)$ are the horizontal wavenumber and wind vectors with components oriented in the zonal and meridional directions, respectively.

We then estimate the vertical wavelength of the events by applying the gravity wave dispersion relation, which constrains the horizontal and vertical wavenumbers, and the wave frequency as $m^2 = \frac{(N^2 - \omega^2)}{(\omega^2 - f^2)} k_h^2$, where $m = 2\pi/\lambda_z$ is the vertical wavenumber, N is the Brunt-Väisälä frequency, and f the inertial frequency. In the calculations that follow, we have assumed a Brunt-Väisälä period of 5.5 min ($N = 0.01904$ rad/sec) and an inertial period of 14.8 hours ($f = 0.11816 \times 10^{-3}$ rad/sec) for Kühlungsborn latitude (54.1°N).

The wave occurring on Nov. 3–4 has $k_x \sim 0$, $k_y = -0.7 \times 10^{-3}$ cycles/km (i.e., $\lambda_y \sim 1365$ km), and $\omega_o = 0.215$ cycles/hour estimated from the keogram spectra. The unfiltered, weighted background wind field over the observatory had components $u = 28.5$ m/s and $v = -1.4$ m/s at 2315 UTC, the instant when the wave was in the dimmer phase of its cycle in the airglow. Applying then the Doppler correction, we estimate an intrinsic frequency $\omega = 0.211$ cycles/hour for the wave. Finally, using the dispersion relation, we derive a vertical wavelength of $\lambda_z = 25.1 \pm 1.0$ km for the Nov. 3–4 wave, which compares well with the value of $\lambda_z = 25.6 \pm 1.0$ km obtained in Section 3.2 by visual inspection of Fig. 10.

Likewise, the Nov. 6–7 wave has $k_x = 0.2441 \times 10^{-3}$ cycles/km (i.e., $\lambda_x \sim 4096$ km), $k_y \sim 0$, and $\omega_o = 0.11$ cycles/hour. Applying once again the Doppler correction for background wind components of $u = 26.0$ m/s and $v = -30.0$ m/s at 2326

Atmospheric
Chemistry
and Physics
Discussions
Open Access
EGU

320　UTC, we obtain an intrinsic frequency of $\omega = 0.087$ cycles/hour. From the dispersion relation we then estimate $\lambda_z = 20.5 \pm 1$ km for this wave, which also agrees with the measured value of $\lambda_z = 21.3 \pm 1$ km from Fig. 10.

　　We also estimate the momentum flux by using again the methodology described in Vargas et al. (2007) along with the intrinsic parameters calculated for the large-scale waves seen in the airglow. The wave amplitudes relative to the mean airglow brightness are $I'_\% = 36.5\%$ (Nov. 3–4 @ 2130 UTC) and $I'_\% = 47.9\%$ (Nov. 6–7 @ 0030 UTC). The vertical wavelengths

325　calculated earlier for each wave and their perturbations in brightness permit estimation of their perturbations at temperatures of $T'_\% = 9.1\%$ (Nov. 3–4) and $T'_\% = 13.7\%$ (Nov. 3–4) using Eq. 12 of Vargas et al. (2007) for the cancellation factor $CF = \frac{I'_\%}{T'_\%} = 4.6 - 3.7e^{0.006(\lambda_z - 6)}$, which is a function of the vertical wavelengths of the waves. Then, taking the acceleration due to gravity as $g = 9.5$ m/s in the mesosphere and using Eq. 13 in Vargas et al. (2007) for the momentum flux, $F_M = -\frac{1}{2}\frac{\omega^2 g^2 m}{N^4 k}|\frac{T'_\%}{100}|^2$, we find $F_M = 21.2$ m^2/s^2 for the wave on Nov. 3–4, and $F_M = 29.6$ m^2/s^2 for the wave on Nov. 6–7. Table 3 shows a summary

330　of the main features of the large-scale waves as discussed above.

　　Based on the momentum flux values of the large-scale waves, we also infer the flux divergence of the southward-traveling wave on Nov. 3–4 that could have caused a deceleration of $\sim$43 m/s/day in the meridional flow by reaching a breaking or dissipation level in its vertical propagation path. Similarly, the wave on Nov. 6–7 would cause a deceleration of $\sim$38 m/s/day in the zonal flux in the breaking or dissipation level. We confirm again that the large-scale waves, having larger amplitudes, would

335　have a greater impact on the mean flow than small-scale waves, even though these oscillatory modes are seen less frequently in mesospheric measurements than their small-scale counterparts.

　　According to Vargas et al. (2019), only a minority of waves seen in the airglow ($\sim$5 %) are in non-dissipating regime, with the majority of the gravity waves presenting strong dissipation and transferring momentum within less than two atmosphere scale heights (12-14 km). Thus, the large momentum flux waves discussed here are likely to present dissipative or breaking

340　characteristics given their larger amplitudes.

　　Recently, Vadas and Becker (2018) have modeled the evolution of mountain waves over the Antarctic Peninsula after observational results of large-scale, long-period waves seen in the mesosphere (Chen et al., 2013, 2016) attributed to an unbalanced flow in the lower stratosphere. This imbalance excited upward (downward) propagating oscillations from the knee of fishbone-like structures at 40 km altitude, which are associated with the excitation of secondary waves from the breaking of extensive

345　mountain wave structures. Although other modeling efforts also attribute the excitation of non-primary waves to localized turbulence eddies from gravity wave breaking (e.g., Heale et al., 2020), we believe that the large-scale waves observed in this study are the product of the Vadas and Becker (2018) mechanism at play in the stratosphere. In fact, preliminary analysis of temperature profiles at 0–90 km altitude acquired by the IAP Rayleigh Lidar system on Nov. 6–7 revealed fishbone structures at 40-45 km, resembling the predictions of Vadas and Becker (2018). We will investigate this possible connection in detail in a

350　separate paper; specifically, we will identify the primary wave sources in the vicinity of IAP during SIMONe–2018, and trace the observed large-scale waves back to their excitation altitude (the fishbone knee region) at 40-45 km revealed in the filtered lidar temperatures.

5 Conclusions

In this paper, gravity waves of small and large horizontal scales were characterized by their intrinsic wave parameters, ampli-
355   tudes, momentum fluxes, and momentum flux divergences. We have focused the analysis on data recorded simultaneously by
an airglow all-sky camera, multistatic specular meteor radar, and TIMED/SABER satellite to obtain a more extensive collection
of complementary information about the state of the mesosphere region over the observatory during the campaign. To uncover
small horizontal scale features, we have used an auto-detection method to process all-sky airglow images and background
meteor radar winds. Large-scale waves were characterized by spectral analysis of airglow keograms and altitude vs. time cross
360   section of filtered wind fluctuations.

Our results indicate that 11% of all detected gravity wave events have large amplitudes and carry 50% of the total momentum
flux estimated during the SIMONe–2018. These fewer wave events could impart mean flow decelerations of 21–43 m/s/day
toward the wave propagation direction at breaking or dissipation levels. If these high-amplitude waves are of secondary wave
generation origin due to their set intrinsic wave features, our results permit verification of the significance of secondary waves
365   in the mesosphere and lower thermosphere dynamics via excitation of large momentum flux gravity waves.

Given the relatively large vertical and horizontal wavelengths of the observed large-scale waves, there is a possibility that
these events are the product of secondary wave excitation via the mechanism identified by Vadas and Becker (2018). This
possibility is supported by stratosphere fishbone structures uncovered in filtered lidar temperatures collected over the IAP
observatory. A complete analysis of these structures will be given in a separate paper, in which we also plan to show the origin
370   of the primary waves in the troposphere from weather images as well as the presence of non-primary waves in other datasets
such as that of the AIRS on board the AQUA satellite.

Author contributions. FV devised the data processing methods, carried out data analysis, and wrote the manuscript. JLC conceived SIMONe
and ran the campaign. HCA provided preprocessed, filtered meteor radar wind data. MG provided lidar data and revised the manuscript.

Competing interests. None

References

380   Asokan, H. C., Chau, J., Marino, R., Vierinen, J., Vargas, F., Urco, J. M., and Clahsen, M.: Study of second-order statistics in the mesosphere
and lower thermosphere region from multistatic meteor radar observations and gravity wave simulations, Atmospheric Chemistry and
Physics, this issue, 2020.

Becker, E. and Vadas, S. L.: Secondary Gravity Waves in the Winter Mesosphere: Results From a High-Resolution Global Circulation Model,
Journal of Geophysical Research: Atmospheres, 123, 2605–2627, 2018.

385   Chau, J. L., Stober, G., Hall, C. M., Tsutsumi, M., Laskar, F. I., and Hoffmann, P.: Polar mesospheric horizontal divergence and relative
vorticity measurements using multiple specular meteor radars, Radio Science, 52, 811–828, https://doi.org/10.1002/2016RS006225, http:
//dx.doi.org/10.1002/2016RS006225, 2017.

Chau, J. L., Urco, J. M., Vierinen, J. P., Volz, R. A., Clahsen, M., Pfeffer, N., and Trautner, J.: Novel specular meteor radar systems using
coherent MIMO techniques to study the mesosphere and lower thermosphere, Atmospheric Measurement Techniques, 12, 2113–2127,

390   2019.

Chen, C., Chu, X., McDonald, A. J., Vadas, S. L., Yu, Z., Fong, W., and Lu, X.: Inertia-gravity waves in Antarctica: A case study using
simultaneous lidar and radar measurements at McMurdo/Scott Base (77.8 °S, 166.7 °E), Journal of Geophysical Research: Atmospheres,
118, 2794–2808, 2013.

Chen, C., Chu, X., Zhao, J., Roberts, B. R., Yu, Z., Fong, W., Lu, X., and Smith, J. A.: Lidar observations of persistent gravity waves with
395   periods of 3–10 h in the Antarctic middle and upper atmosphere at McMurdo (77.83 °S, 166.67 °E), Journal of Geophysical Research:
Space Physics, 121, 1483–1502, 2016.

Fritts, D. C. and Alexander, M. J.: Gravity wave dynamics and effects in the middle atmosphere, Reviews of Geophysics, 41, 2003.

Fritts, D. C., Vadas, S. L., Wan, K., and Werne, J. A.: Mean and variable forcing of the middle atmosphere by gravity waves, Journal of
Atmospheric and Solar-Terrestrial Physics, 68, 247 – 265, 2006.

400   Gobbi, D., Takahashi, H., Clemesha, B., and Batista, P.: Equatorial atomic oxygen profiles derived from rocket observations of OI 557.7 nm
airglow emission, Planetary and Space Science, 40, 775 – 781, 1992.

Greer, R., Murtagh, D., McDade, I., Dickinson, P., Thomas, L., Jenkins, D., Stegman, J., Llewellyn, E., Witt, G., Mackinnon, D., and
Williams, E.: ETON 1: A data base pertinent to the study of energy transfer in the oxygen nightglow, Planetary and Space Science, 34,
771 – 788, 1986.

405   Heale, C. J., Bossert, K., Vadas, S. L., Hoffmann, L., Dörnbrack, A., Stober, G., Snively, J. B., and Jacobi, C.: Secondary Gravity Waves
Generated by Breaking Mountain Waves Over Europe, Journal of Geophysical Research: Atmospheres, 125, e2019JD031 662, 2020.

Holton, J. R.: The generation of mesospheric planetary waves by zonally asymmetric gravity wave breaking, J.atmos., 41, 3427–3430, 1984.

Houghton, J. T.: The stratosphere and mesosphere, Quarterly Journal of the Royal Meteorological Society, 104, 1–29, 1978.

Li, Z.: An observational investigation on gravity wave characteristics and propagation in the lower stratosphere and mesopause, Ph.D. thesis,
410   University of Illinois at Urbana-Champaign, 2011.

Li, Z., Liu, A. Z., Lu, X., Swenson, G. R., and Franke, S. J.: Gravity wave characteristics from OH airglow imager over Maui, Journal of
Geophysical Research: Atmospheres, 116, 2011.

Melo, S., Takahashi, H., Clemesha, B., Batista, P., and Simonich, D.: Atomic oxygen concentrations from rocket airglow observations in the
equatorial region, Journal of Atmospheric and Terrestrial Physics, 58, 1935–1942, 1996.

415   Solomon, S., R., G. R., Edgeworth, M. M., Adrian, P. J., L., T., and Robert, W.: Current understanding of mesospheric transport processes,
       Philosophical Transactions of the Royal Society of London. Series A, Mathematical and Physical Sciences, pp. 655–666, 1987.

Stober, G. and Chau, J. L.: A multistatic and multifrequency novel approach for specular meteor radars to improve wind measurements in the
       MLT region, Radio Science, 50, 431–442, https://doi.org/10.1002/2014RS005591, http://doi.wiley.com/10.1002/2014RS005591, 2015.

Swenson, G. R. and Espy, P. J.: Observations of 2-dimensional airglow structure and Na density from the ALOHA, October 9, 1993 'storm
420   flight', Geophysical Research Letters, 22, 2845–2848, 1995.

Tang, J., Kamalabadi, F., Franke, S. J., Liu, A. Z., and Swenson, G. R.: Estimation of gravity wave momentum flux with spectroscopic
       imaging, IEEE Transactions on Geoscience and Remote Sensing, 43, 103–109, 2005.

Urco, J. M., Chau, J. L., Milla, M. A., Vierinen, J. P., and Weber, T.: Coherent MIMO to improve aperture synthesis radar imag-
       ing of field-aligned irregularities: First results at Jicamarca, IEEE Transactions on Geoscience and Remote Sensing, 56, 2980–2990,
425   https://doi.org/10.1109/TGRS.2017.2788425, 2018.

Urco, J. M., Chau, J. L., Weber, T., Vierinen, J., and Volz, R.: Sparse signal recovery in MIMO specular meteorradars with waveform
       diversity, IEEE Trans. Geosci. Remote Sensing, p. 1, papers2://publication/uuid/3BE7DFC6-C58D-4567-AB89-92B77BC87721, 2019.

Vadas, S. L. and Becker, E.: Numerical Modeling of the Excitation, Propagation, and Dissipation of Primary and Secondary Gravity Waves
       during Wintertime at McMurdo Station in the Antarctic, Journal of Geophysical Research: Atmospheres, 123, 9326–9369, 2018.

430   Vadas, S. L., Zhao, J., Chu, X., and Becker, E.: The Excitation of Secondary Gravity Waves From Local Body Forces: Theory and Observa-
       tion, Journal of Geophysical Research: Atmospheres, 123, 9296–9325, 2018.

Vargas, F.: Uncertainties in gravity wave parameters, momentum fluxes, and flux divergences estimated from multi-layer measurements of
       mesospheric nightglow layers, Advances in Space Research, 63, 967 – 985, 2019.

Vargas, F., Swenson, G., Liu, A., and Gobbi, D.: O(1S), OH, and O2(b) airglow layer perturbations due to AGWs and their implied effects
435   on the atmosphere, Journal of Geophysical Research: Atmospheres, 112, 2007.

Vargas, F., Gobbi, D., Takahashi, H., and Lima, L. M.: Gravity wave amplitudes and momentum fluxes inferred from OH airglow intensities
       and meteor radar winds during SpreadFEx, Annales Geophysicae, 27, 2361–2369, 2009.

Vargas, F., Swenson, G., and Liu, A.: Evidence of high frequency gravity wave forcing on the meridional residual circulation at the mesopause
       region, Advances in Space Research, 56, 1844 – 1853, 2015.

440   Vargas, F., Swenson, G., Liu, A., and Pautet, D.: Evidence of the excitation of a ring-like gravity wave in the mesosphere over the Andes
       Lidar Observatory, Journal of Geophysical Research: Atmospheres, 121, 8896–8912, 2016.

Vargas, F., Yang, G., Batista, P., and Gobbi, D.: Growth Rate of Gravity Wave Amplitudes Observed in Sodium Lidar Density Profiles and
       Nightglow Image Data, Atmosphere, 10, 2019.

Vargas, F., Brum, C., Terra, P., and Gobbi, D.: Mean Zonal Drift Velocities of Plasma Bubbles Estimated from Keograms of Nightglow
445   All-Sky Images from the Brazilian Sector, Atmosphere, 11, 2020.

Vierinen, J., Chau, J. L., Pfeffer, N., Clahsen, M., and Stober, G.: Coded continuous wave meteor radar, Atmospheric Measurement Tech-
       niques, 9, 829–839, https://doi.org/10.5194/amt-9-829-2016, https://www.atmos-meas-tech.net/9/829/2016/, 2016.

Vierinen, J., Chau, J. L., Charuvil, H., Urco, J. M., Clahsen, M., Avsarkisov, V., Marino, R., and Volz, R.: Observing Mesospheric Turbulence
       With Specular Meteor Radars: A Novel Method for Estimating Second-Order Statistics of Wind Velocity, Earth and Space Science, 6,
450   1171–1195, 2019.

Vincent, R. A. and Alexander, M. J.: Balloon-borne observations of short vertical wavelength gravity waves and interaction with QBO winds,
       Journal of Geophysical Research: Atmospheres, n/a, e2020JD032 779, 2020.

Table 1. Configuration of the All-sky imager system used to collect airglow images during the SIMONe–2018 Campaign. Airglow images of the campaign are available at http://sirius.bu.edu/data/.

Filter	Emission	Wavelength (nm)	Integration Time (sec)
RG695	OH	695.0–1050.0	15
6050C	Background OH	605.0	120
5893C	NaD	589.3	120
8660C	$O_2(0,1)$	864.5	120
5577C	$O(^1S)$	557.7	120
6300C	$O(^1D)$	630.0	120

Table 2. Centroid, peak, and FWHM of the OH, O_2, and $O(^1S)$ layers measured and calculated using TIMED/SABER data collected near Kühlungsborn during SIMONe–2018 campaign.

Emission	Wavelength	Origin	Layer Centroid (km)	Layer Peak (km)	FWHM (km)
OH(A)	2.1 μm	SABER	~87.3	~86.4	~14.3
OH(B)	1.6 μm	SABER	~85.8	~84.8	~12.5
OH(8,3)	727.3 nm	simulation	~89.4	~86.5	~18.7
O_2(0-1)	864.5 nm	simulation	~91.1	~88.0	~14.6
$O(^1S)$	557.7 nm	simulation	~93.3	~91.4	~16.7

Table 3. Estimated features of the large-scale waves observed in the airglow and meteor radar wind data.

Date	λ_h (km)	λ_z (km)	τ_o (h)	τ_i (h)	c_o (m/s)	c_i (m/s)	I' (%)	T' (%)	F_M (m^2/s^2)
Nov. 3–4	1365	25.1	4.6	4.7	81.6	80.3	36.5	9.1	21.2
Nov. 6–7	4096	20.5	9.1	11.5	125.2	99.1	47.9	13.7	29.6

Atmospheric
Chemistry
and Physics
Discussions
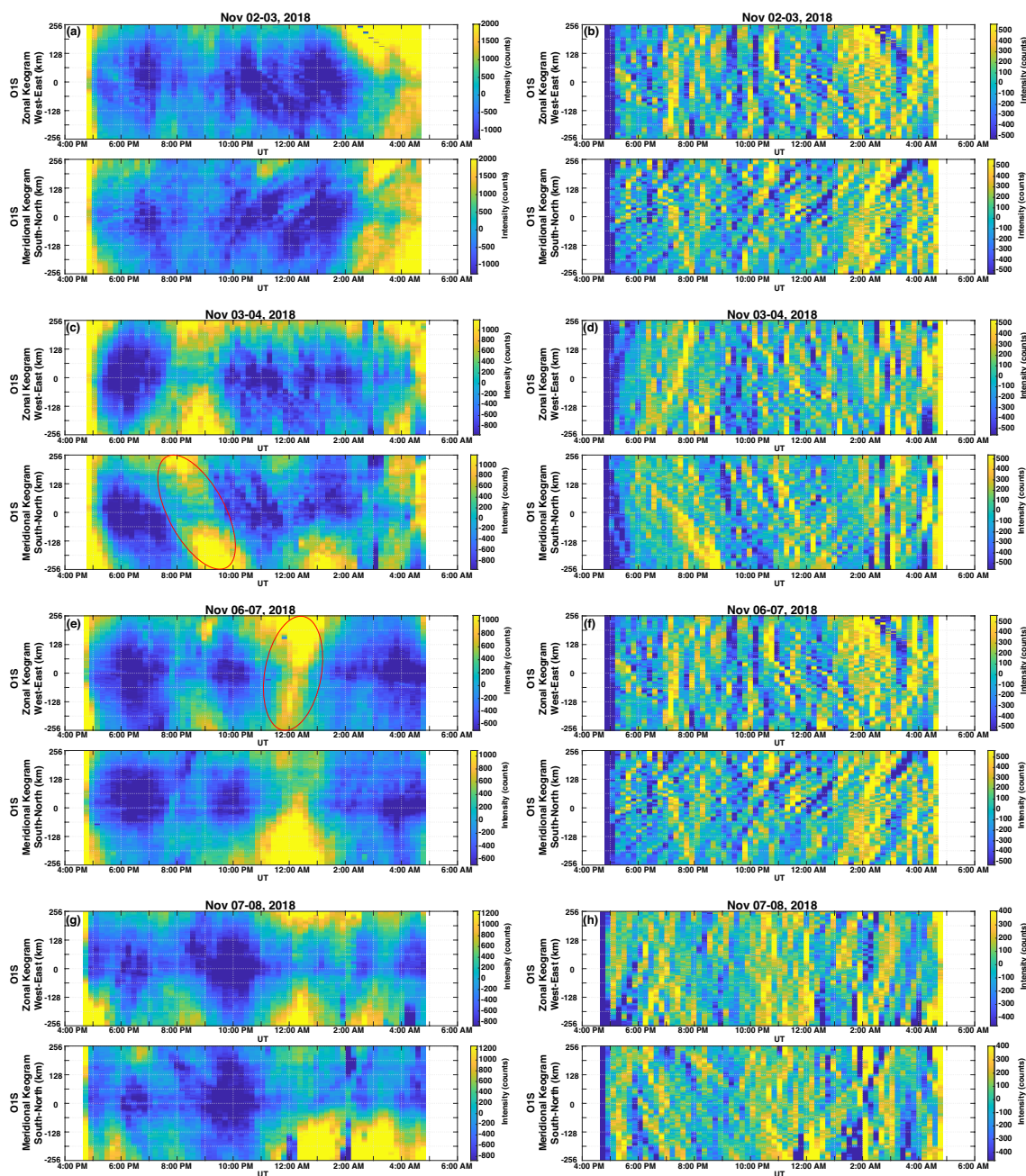
Figure 1. Composite keograms of O(^{1}S) airglow images taken on clear nights during the SIMONe–2018 campaign. The keograms in panels (a), (c), (e), and (f) were built using light frame images, while keograms in panels (b), (d), (f), and (g) were built using time-difference images. Time difference keograms show short-period waves in higher contrast, while light frame keograms show mainly long-period oscillations. Note the enhanced airglow brightness (red ellipses) on Nov. 3–4 (meridional keogram) and Nov. 6–7 (zonal keogram) associated with large-scale gravity waves also seen in filtered wind fluctuations of Figure 2.

Atmospheric
Chemistry
and Physics
Discussions

Open Access

EGU
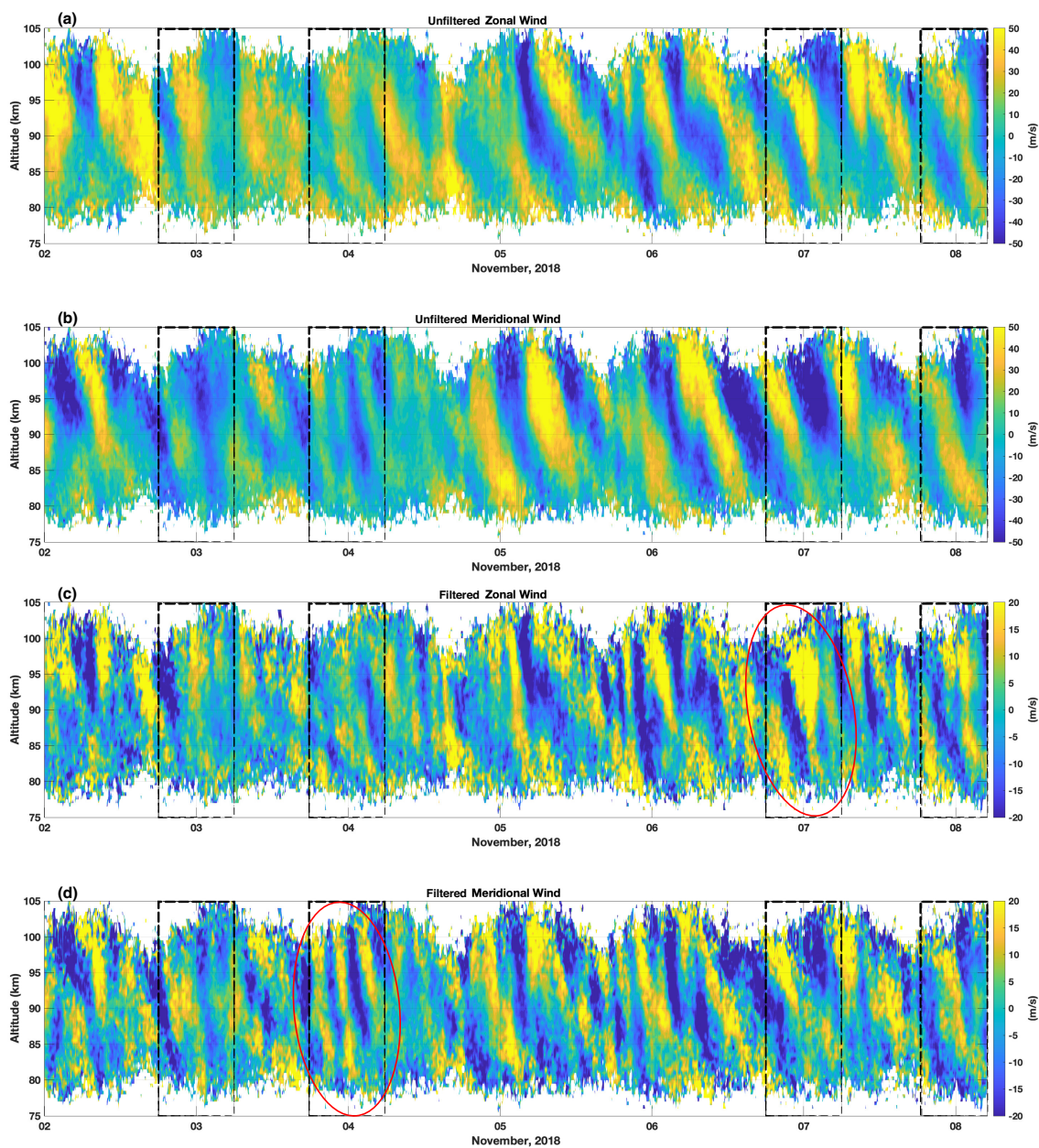
Figure 2. (a) Zonal and (b) meridional wind measurements for the duration of the SIMONe–2018 campaign generated by the MSMR network. Note the dominance of the semidiurnal tide on the horizontal wind. (c) and (d) High-pass filtered zonal and meridional wind fluctuations of periods >5 hours. Note the presence of coherent gravity wave features (red ellipses) on Nov. 3–4 in the meridional wind fluctuations and on Nov. 6–7 in the zonal wind fluctuations coincident with enhanced keogram brightness for the same nights in Figure 1. Black dashed boxes indicate hours of simultaneous operation of the ASI and MSMR systems.
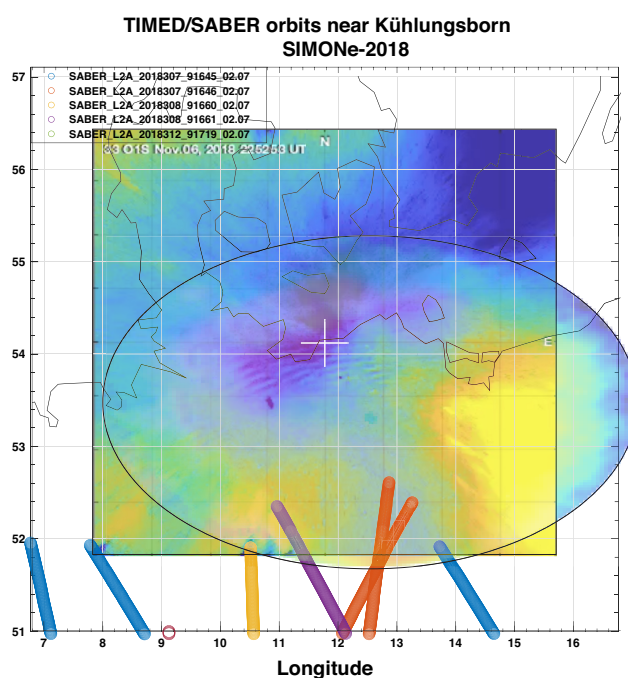
Figure 3. Individual TIMED/SABER satellite orbits near Kühlungsborn during the SIMONe–2018 campaign. The colored lines represent the locations where vertical atmospheric profiles were calculated. The field of view of 512x512 km^2 of the airglow camera projected at $\sim$ 95 km is indicated by the O(^{1}S) image mapped onto geographic coordinates, while the ellipse indicates the field of view of the MSMR system. The white cross near the center indicates the coordinates of the Kühlungsborn observatory.
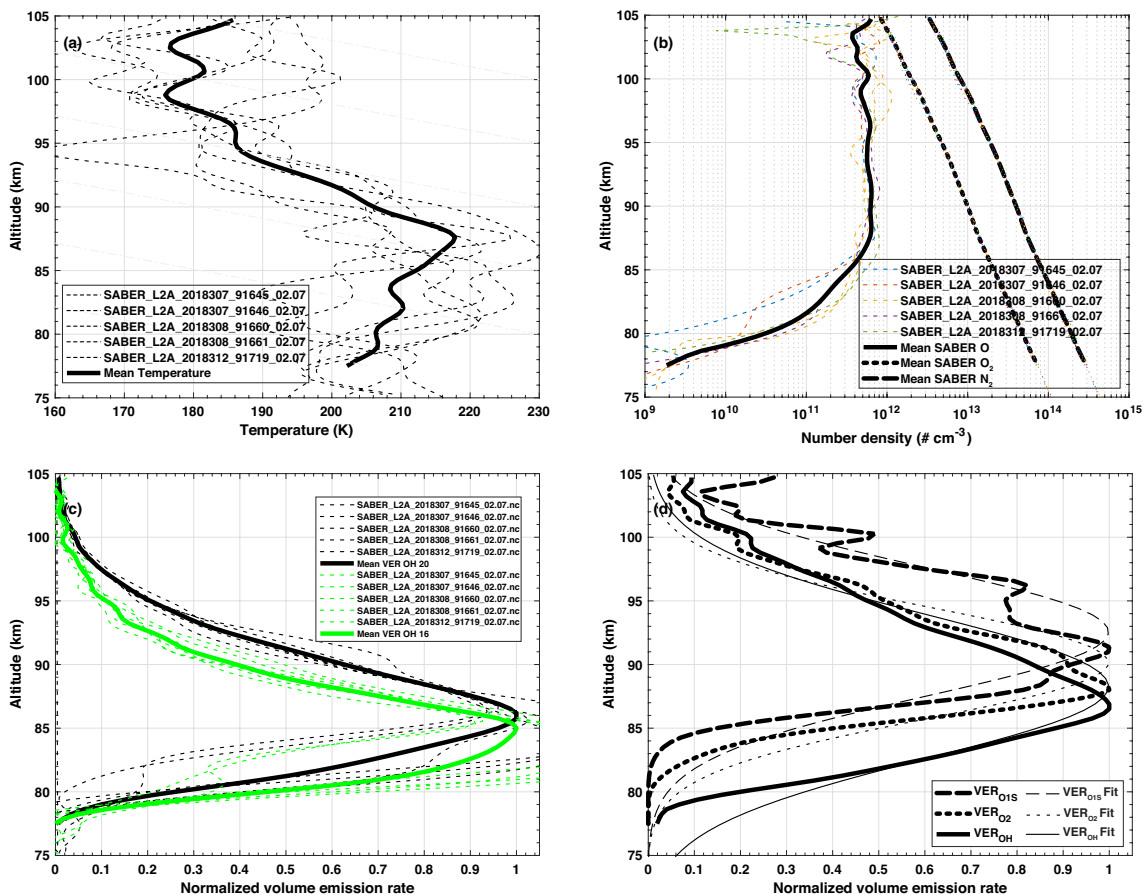
Figure 4. (a) Temperature, (b) atomic oxygen, molecular oxygen, molecular nitrogen number densities, and (c) OH20 (2.1 μm OH(A)) and OH16 (1.6 μm OH(B)) volume emission rates collected by TIMED/SABER satellite near Kühlungsborn during the SIMONe–2018 campaign within four degrees of latitude or longitude of the observatory. The dotted lines indicate individual orbits of the satellite, while thick lines indicate the mean of the individual orbits. (d) Calculated volume emission rate for OH(8,3), $O_2(0,1)$, and O(^{1}S) layers (thick black lines) using SABER mean profiles in panels (a) and (b). Thin black lines in (d) are Gaussian fits of the calculated VER profiles. Individual VER airglow layer features for both measured and calculated VER are in Table 2.
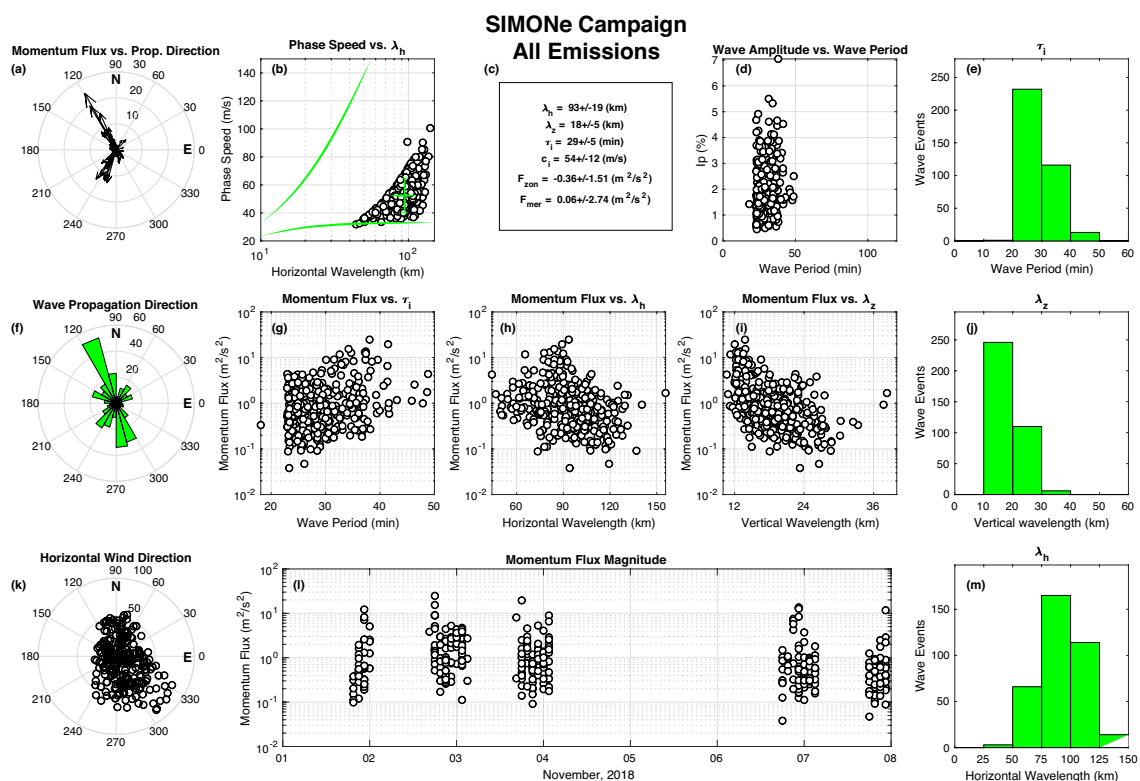
Figure 5. Short-period wave parameters obtained from OH, O_2, $O(^1S)$, and Na airglow image analysis using the auto-detection method (Vargas et al., 2009; Vargas, 2019). Separate plots of waves detected in each emission are in the supplementary files of this paper.
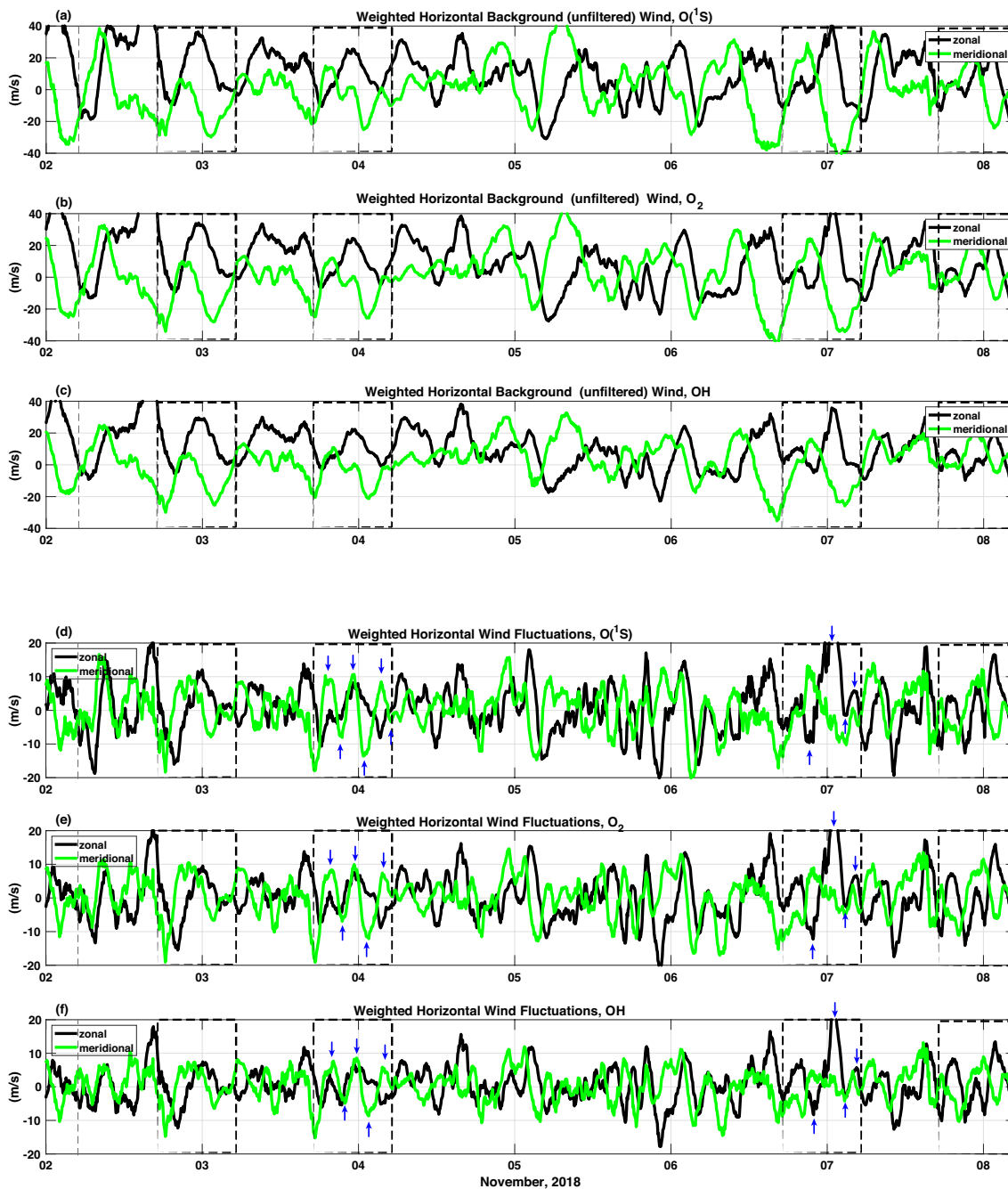
Figure 6. (a) O(^{1}S), (b) O$_2$, and (c) OH volume emission rate weighted zonal and meridional background (unfiltered) winds. (d) O(^{1}S), (e) O$_2$, and (f) OH volume emission rate weighted zonal and meridional wind fluctuations. The vertical blue arrows indicate coherent wind fluctuations also seen in the airglow brightness. The dashed black rectangles indicate the all-sky imager operation time during SIMONe–2018 clear sky nights.
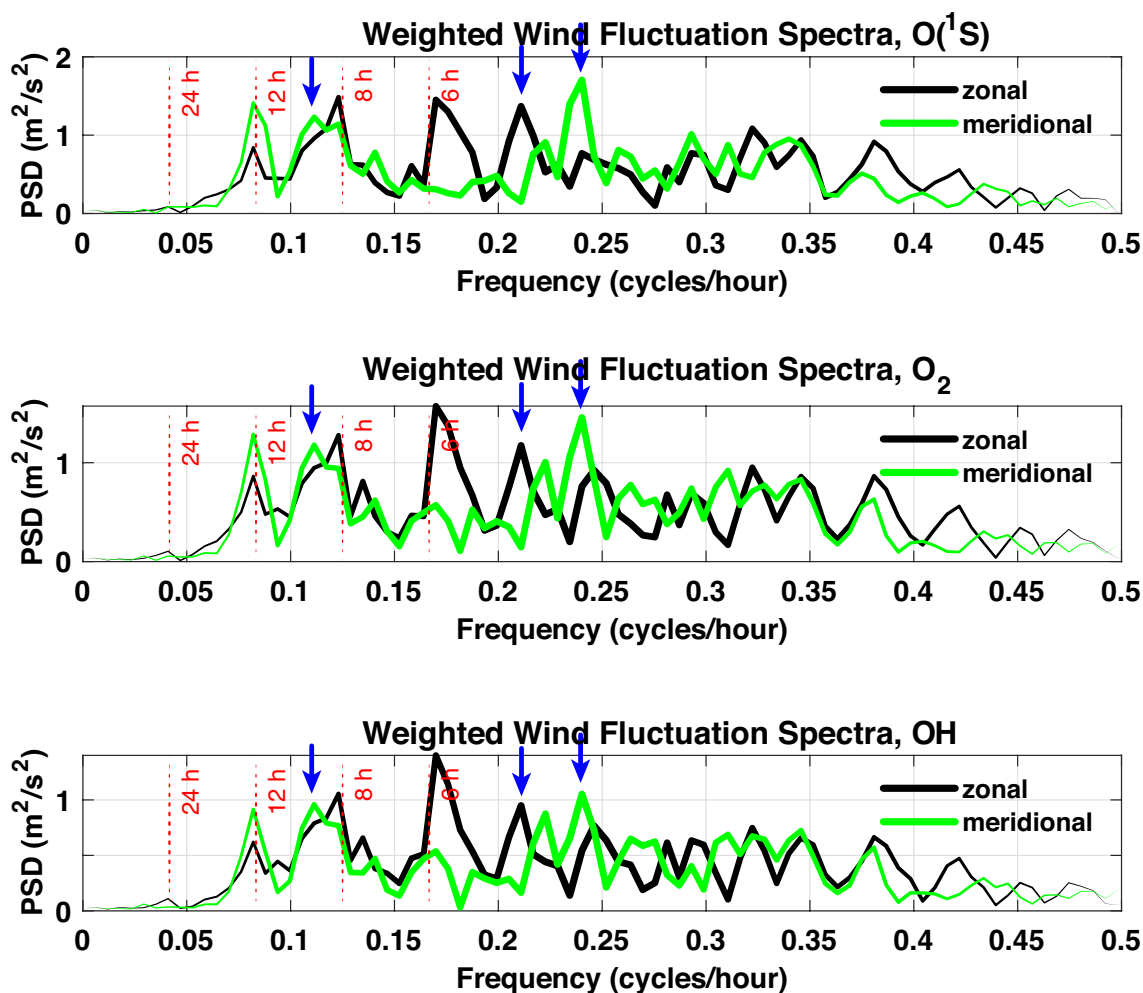
Figure 7. Spectra of weighted zonal and meridional wind fluctuation of Fig. 6. The dashed red lines indicate tidal periods present in the signal. The horizontal range represents periods >2 hours. The vertical blue arrows indicate wave frequencies of persisting wave structures also seen in the airglow brightness.
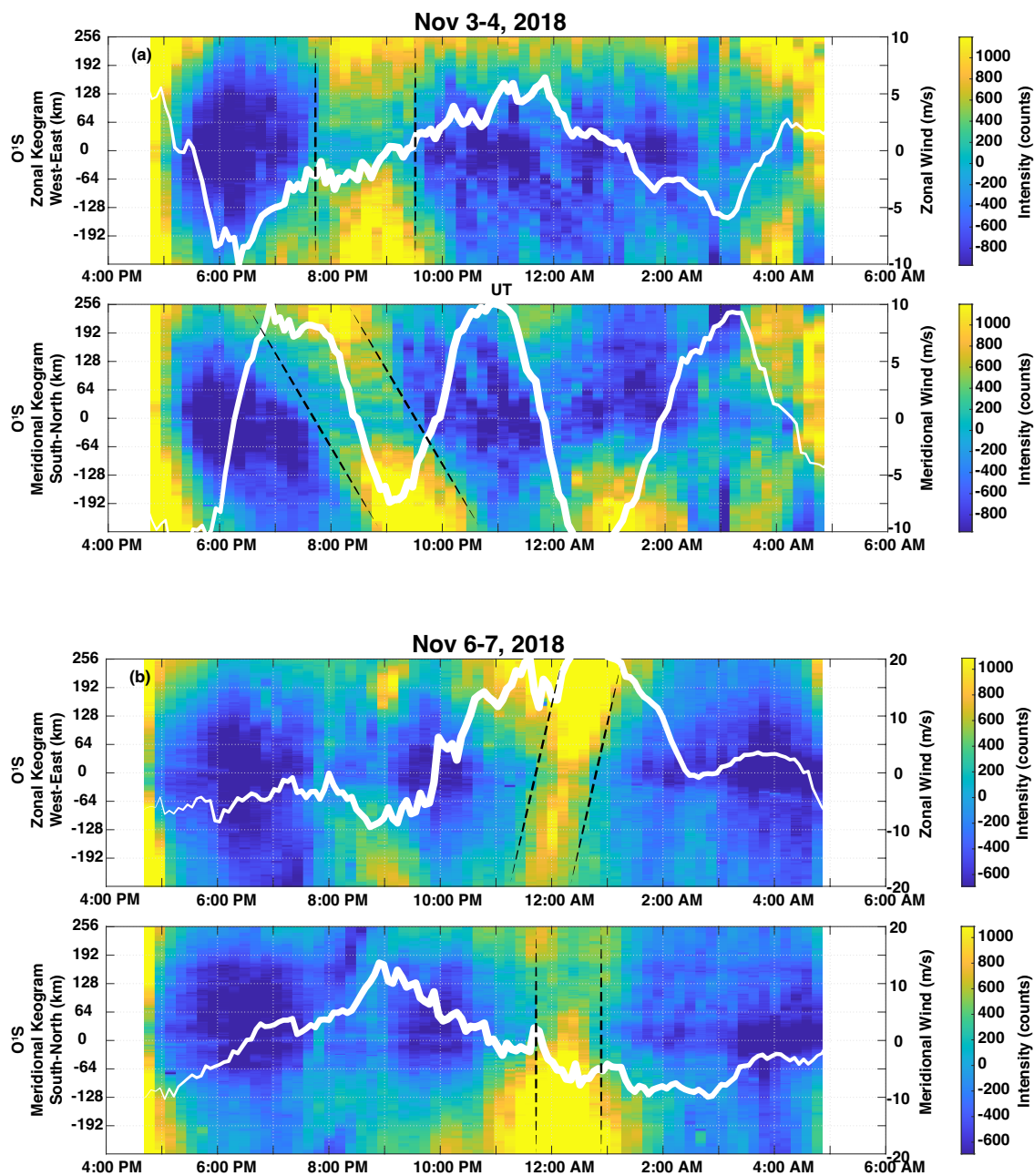
Figure 8. Enhanced contrast keograms of O(^{1}S) airglow for (a) Nov. 3–4 and (b) Nov. 6–7, 2018. The keogram of Nov. 3–4 shows a strong, large-scale gravity wave at 2000-2200 UTC heading south. A large-scale wave is also seen on Nov. 6–7 propagating eastward at 0000 UTC. The white lines overlaid on the keograms indicate wind fluctuations weighted by the volume emission rate of the O(^{1}S) layer.
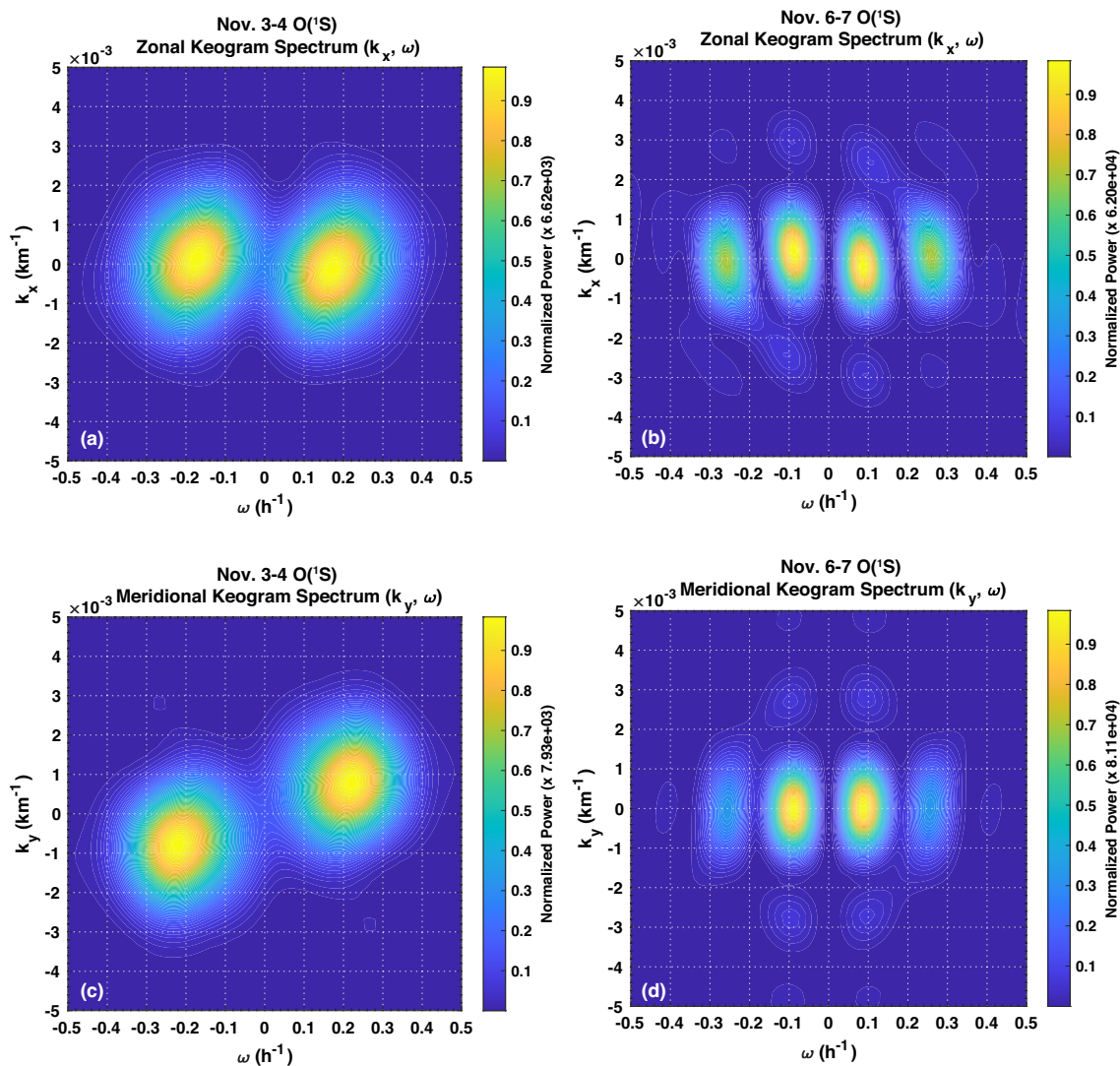
Figure 9. Composite (k_x, ω) and (k_y, ω) spectra of the keograms in Fig. 8 for the nights of Nov. 3–4 (panels a and c) and Nov. 6–7 (panels b and d).
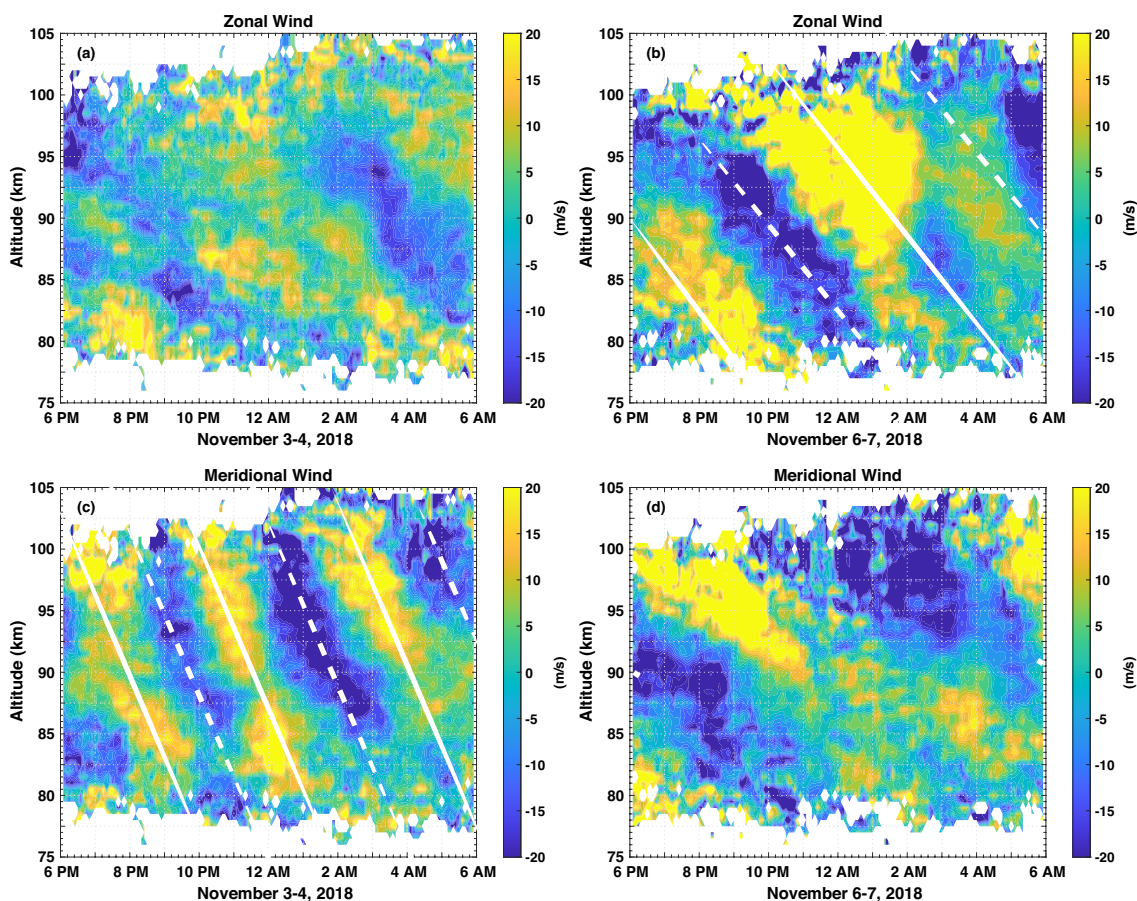
Figure 10. Time-altitude cross section of the zonal and meridional weighted wind fluctuations for the nights of Nov. 3–4 and Nov. 6–7, 2018. The continuous (dashed) white lines indicate crests (troughs) of the oscillations as well as the descending phase (ascending energy propagation) of the waves. Notice the coherent ∼4.0 hours period gravity wave oscillation on Nov. 3–4 with vertical wavelength of 25.6 km. The wave period gets slightly longer by the end of the night as the wave tilts to shallow angles with respect to the horizontal. The wave on Nov. 6–7 in the zonal wind cross section corresponds to an ∼21.3 km vertical wavelength, ∼8 hours period wave.